ADVANCED ENGINEERING MATERIALS
www.aem-journal.com

Flow Behavior and Microstructure of Hot-Worked TiNbTaVW Refractory High-Entropy Alloy

Olufemi Sylvester Bamisaye, Nthabiseng Maledi, Josias Van der Merwe, Desmond Klenam, and Michael Bodunrin*

The high-temperature deformation behavior of an equiatomic TiNbTaVW refractory high entropy alloy (RHEA) was studied at temperatures of 950, 1000, and 1050 °C and a strain rate of 10^{-3} s^{-1}. The flow stress, high-temperature strength, and softening mechanisms were analyzed and compared with the IN718 nickel-based superalloy. The results indicate that the flow stress of both TiNbTaVW and IN718 is sensitive to deformation temperature, with high temperatures resulting in reduced flow stress. Globular grains and elongated grains were observed at 950 and 1000 °C for TiNbTaVW, signifying both dynamic recovery and dynamic globularization as the softening mechanisms. Globular grains were only observed at 1050 °C for TiNbTaVW, signifying dynamic globularization as the softening mechanism. The TiNbTaVW RHEA has a higher temperature strength of 910, 870, and 658 MPa compared to the IN718 alloy with 72, 87, and 61 MPa at 950–1000 °C/10^{-3} s^{-1}. By demonstrating comparable or superior performance in specific aspects, RHEAs can be considered in the near future for potential applications traditionally dominated by nickel-based superalloys.

1. Introduction

For over a decade, there has been a persistent demand for new materials with excellent mechanical properties to meet the requirements of various high-temperature structural applications, particularly in the aerospace industry. Currently, advanced materials, such as nickel-based superalloys, are among the main commercially used alloys. However, these materials are approaching their design limits as operating temperatures get closer to their melting points.[1,2] Therefore, there is a need for promising materials with high-temperature mechanical properties at or above 1200 °C. A new alloy design concept known as high-entropy alloys[3] has been utilized to develop novel refractory metals containing several principal elements at near or equiatomic concentrations.[4] Refractory high-entropy alloys (RHEAs) have attracted specific interest as potential candidates for higher-temperature functional materials due to their high-temperature strength, hardness, and wear resistance.[5–11] Understanding the high-temperature behavior of RHEAs is important before they can be used for structural and functional applications. Thermomechanical processing of RHEAs at high temperatures is an effective method of shaping and modifying the microstructure and properties after casting.[12,13]

In other metallic alloys, desirable softening mechanisms like dynamic recovery (DRV) and dynamic recrystallization (DRX) can occur during hot deformation in RHEAs.[5,14–19] Eleti et al.[17] deformed the HfNbTaTiZr RHEA at 1000 °C/10^{-3} s^{-1} and observed significant bulging along grain boundaries, leading to the emergence of DRX grains. Wang et al.[20] studied the isothermal compression of the NbZrTiTa RHEA at 900–1200 °C/10^{-3} s^{-1} and identified new fine grains near deformed grain boundaries, suggesting DRX. Li et al.[21] found dynamically recrystallized grains when deforming the $Ti_2ZrHfV_{0.5}Ta_{0.2}$ RHEA at 900–1100 °C/10^{-1}–10^{-3} s^{-1}. Bai et al.[19] investigated the isothermal compression behavior of the $TiAlVNb_2$ RHEA at 1000–1200 °C/10^{-1}–10^{-3} s^{-1} and identified the softening mechanisms as DRV and DRX. Unsafe deformation behaviors such as fracture, flow localization, wedge cracking, and adiabatic shear banding have also been observed in RHEAs.[10,22–28] Brittle and fracture behaviors have been found in some hot deformed RHEAs, limiting their deformation to a strain ≤30% and a

O. S. Bamisaye, N. Maledi, J. V. Merwe, D. Klenam, M. Bodunrin
School of Chemical and Metallurgical Engineering
Faculty of Engineering and the Built Environment
University of the Witwatersrand
Johannesburg 2050, South Africa
E-mail: 2503285@students.wits.ac.za

O. S. Bamisaye
Mechanical Engineering Department
Faculty of Air Engineering
Air Force Institute of Technology
800283 Kaduna, Nigeria

N. Maledi, J. V. Merwe, M. Bodunrin
DSI-NRF Centre of Excellence in Strong Materials
University of the Witwatersrand
Johannesburg 2050, South Africa

D. Klenam
Academic Development Unit
Faculty of Engineering and the Built Environment
University of Witwatersrand
Johannesburg 2050, South Africa

The ORCID identification number(s) for the author(s) of this article can be found under https://doi.org/10.1002/adem.202400538.

DOI: 10.1002/adem.202400538

low strain rate of $10^{-3}\,s^{-1}$. Typical RHEAs that have been reported include WTaMoNbTi (25%),[29] NbMoCrTiAl (20%),[23] $W_{0.4}MoNb_xTaTi$ (30%),[10] AlCrNbTiVZr (30%),[28] and $MoNbVTa_x$ (25%).[30]

TiNbTaVW is a single-body-centered-cubic (BCC) phase RHEA known for its high hardness and excellent corrosion resistance in chloride and acidic environments compared to the IN718 alloy.[31] However, the flow behavior, microstructural evolution, and high-temperature strength of the TiNbTaVW RHEA compared to IN718 have not been explored. Therefore, the softening mechanisms for the TiNbTaVW RHEA under high-temperature deformation are unknown. This study aimed to determine the isothermal compression behavior of the TiNbTaVW RHEA at temperatures of 950–1050 °C and a strain rate of $10^{-3}\,s^{-1}$ using the Gleeble 3500 thermomechanical simulator. Emphasis was placed on the flow behavior and microstructural evolution to determine the softening mechanisms and high-temperature strength.

2. Results and Discussion

2.1. Initial Phase and Microstructure

The phases and microstructures of the TiNbTaVW RHEA and IN718 alloy are presented in **Figure 1** and are reproduced from previous work.[31] In Figure 1a, the X-ray diffraction (XRD) analysis result of the TiNbTaVW RHEA shows peaks indexed as the BCC solid solution phase (Im-3 m (229); $a = b = c = 3.2350$ Å), observed within a wide range of 2θ values between 46° and 103°. Also, a small peak at ≈41° was not accounted for because it could not be identified. The scanning electron microscope in backscattered electron (SEM–BSE) image of the TiNbTaVW RHEA exhibits a dendritic microstructure (Figure 1b). The XRD spectra of IN718 in Figure 1c show that γ(Fm-3 m (225); $a = b = c = 3.5920$ Å) and γ'' (Fm-3 m (225); $a = b = c = 3.6150$ Å) are the two major peaks present at a wide range of 2θ values between 51.7° and 111.7°. The γ and γ'' have been reported in some literature on wrought Inconel 718.[32–35] Microstructural analysis of the IN718 alloy shows fine-distributed γ grains and γ'' precipitated grains (Figure 1d). The elemental compositions of TiNbTaVW and IN718 are presented in **Table 1** and **2** and are reproduced from previous work.

2.2. Stress–Strain Behavior

The stress–strain curves of the TiNbTaVW and IN718 obtained at 950 to 1050 °C and a strain rate of $10^{-3}\,s^{-1}$ are shown in **Figure 2**. The flow stress of both TiNbTaVW and IN718 is sensitive to deformation temperature, with high temperatures reducing the flow stress. High temperatures accelerate the movement of grain boundaries and dislocations, leading to softening and decreased stress.[19] At 950 °C, a steady-state flow stress followed

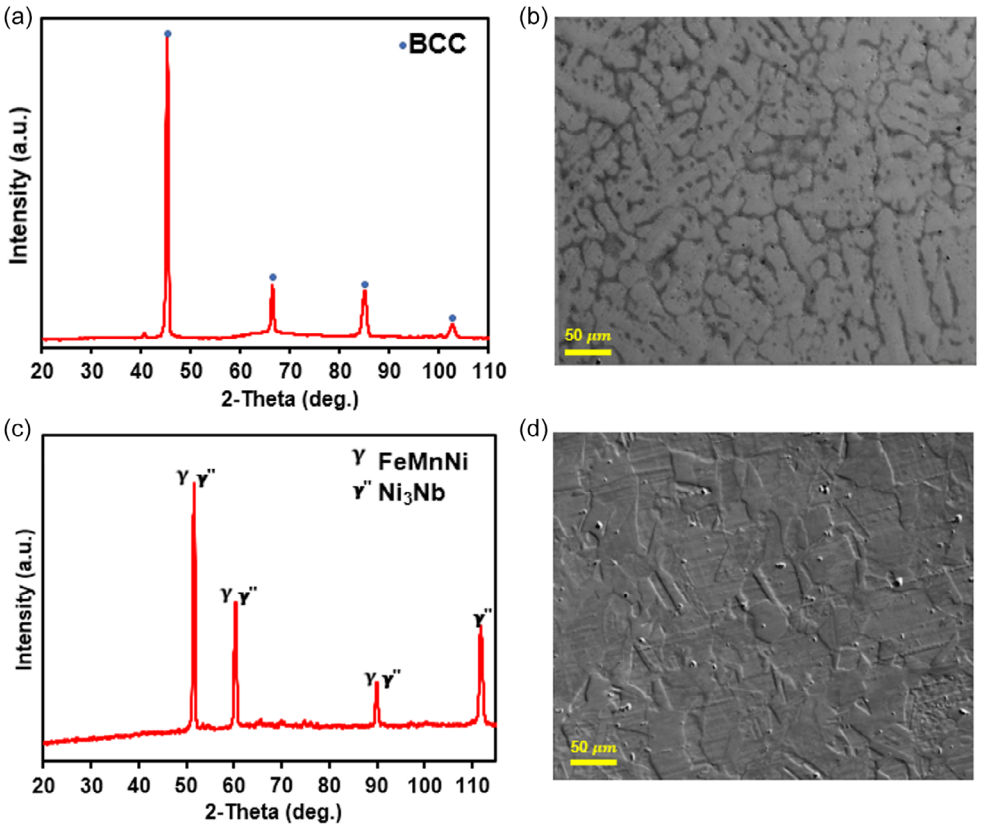

Figure 1. XRD pattern of the phase present in the TiNbTaVW RHEA: a) SEM–BSE image of the TiNbTaVW RHEA; b) XRD pattern of the phase present in the IN718 alloy; and c,d) SEM–BSE image of the IN718 alloy. Reproduced with permission.[31] Copyright 2024, Elsevier B.V.

Table 1. Composition distribution of the TiNbTaVW RHEA (at%). Reproduced with permission.[31] Copyright 2024, Elsevier B.V.

TiNbTaVW RHEA	Element	Ti	Nb	Ta	V	W
–	Actual	19 ± 0.4	20 ± 0.2	21 ± 0.2	20 ± 0.3	20 ± 0.2
	Dendrite (grey)	14 ± 0.8	19 ± 0.5	24 ± 0.5	15 ± 1.1	28 ± 1.9
	Interdendrite (dark)	32 ± 1.5	19 ± 0.3	12 ± 0.8	29 ± 0.6	8.0 ± 1.0

Table 2. Composition distribution of the IN718 alloy (at%). Reproduced with permission.[31] Copyright 2024, Elsevier B.V.

IN718 alloy	Ti	Nb	Fe	Ni	Mn	S	C	Co	Al	Si	P	Cu
–	0.12 ± 0.02	0.22 ± 0.02	57.95 ± 0.1	36.56 ± 0.4	0.5 ± 0.1	0.06 ± 0.1	3.63 ± 0.1	0.14 ± 0.04	0.12 ± 0.02	0.37 ± 0.02	0.1 ± 0.01	0.23 ± 0.01

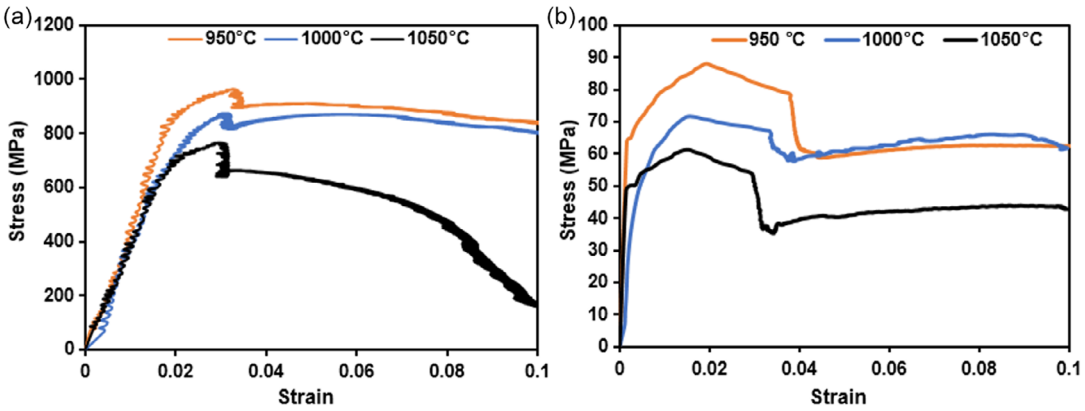

Figure 2. True stress–strain curves at 950–1050 °C and a strain rate of 10^{-3} s^{-1} for a) TiNbTaVW and b) IN718.

by a reduction in flow stress was observed in the TiNbTaVW (Figure 2a). At 1000 °C, a broad peak stress followed by a reduction in flow stress was observed. While at 1050 °C, continuous flow softening was observed in the TiNbTaVW. A broad peak stress has been attributed to DRX,[36,37] while continuous flow softening can suggest dynamic globularization, flow localization, or wedge cracking.[38,39] Continuous flow softening occurs when the rate of softening surpasses the work hardening rate.[40,41] Similarly, at 950 and 1050 °C, the flow curve of the IN718 alloy exhibits a steady-state flow stress (Figure 2b). While at 1000 °C, a steady-state stress followed by a reduction in flow stress was observed. A steady-state flow stress suggests either DRV or DRX.[42,43]

At 950–1050 °C, the flow curves of TiNbTaVW and IN718 at the elastic deformation stage exhibit a behavior characterized by a sudden increase in the flow stress followed by a drop. Similar phenomena have been reported in other alloys such as Ti–6Al–4 V,[44] HfNbTaTiZr,[12] $Ti_2ZrTa_{0.75}$,[45] $AlNbTi_3VZr_{1.5}$,[46] and $Ti_2ZrHfV_{0.5}Ta_{0.2}$.[21] This phenomenon may occur due to dislocation unlocking by solute atoms or the ending of short-range order.[21] Additionally, it could result from a change in strain rate at low strain during the hot deformation experiment.[44] Serrations were detected in the elastic region of the TiNbTaVW flow curve at 950–1050 °C. It was also detected at the plastic region of the TiNbTaVW and IN718 flow curves at 1050 and 1000 °C. Serrations occur due to the repeated pinning and depinning of solute atoms on dislocations.[47–50]

2.3. Microstructural Evolution

The optical and SEM–BSE images of TiNbTaVW and IN718 after deformation at 950, 1000, and 1050 °C at a strain rate of 10^{-3} s^{-1} are presented in **Figure 3**, **4**, and **5**. The deformed TiNbTaVW RHEA did not exhibit localized deformation features such as adiabatic shear bands but only voids (red arrows) at 950 °C (Figure 3a,b). The microstructure of TiNbTaVW at 950 °C comprises globular (black arrows) and elongated grains (blue arrows) (Figure 3a,b). Grain sizes of 44.45 ± 5.0 μm were observed at 950 °C. At higher temperatures and lower strain rates, more time and energy can aid grain boundary migration and eventually promoting DRX. Elongated grains were also observed in some regions of the microstructure, suggesting DRV.

At 950 °C, no cracks or adiabatic shear bands appear in the microstructure of IN718 (Figure 3c,d). Equiaxed (black arrows) and elongated grains (blue arrows) are present in the microstructure at 950 °C, with grain sizes of 40.3 ± 6.9 μm. Equiaxed grains (black arrows) are commonly seen in metals and alloys dynamically recrystallized during hot compression.[12]

At 1000 °C, the TiNbTaVW RHEA comprises globular (black arrows) and elongated grains (blue arrows) (Figure 4a,b). Some of the elongated grains are rotated in certain regions of the microstructure. The elongated grains suggest DRV. Finer grains (35.01 ± 4.1 μm) were observed compared to grains at 950 °C (44.45 ± 5.0 μm). Voids (red arrows) are still found in some

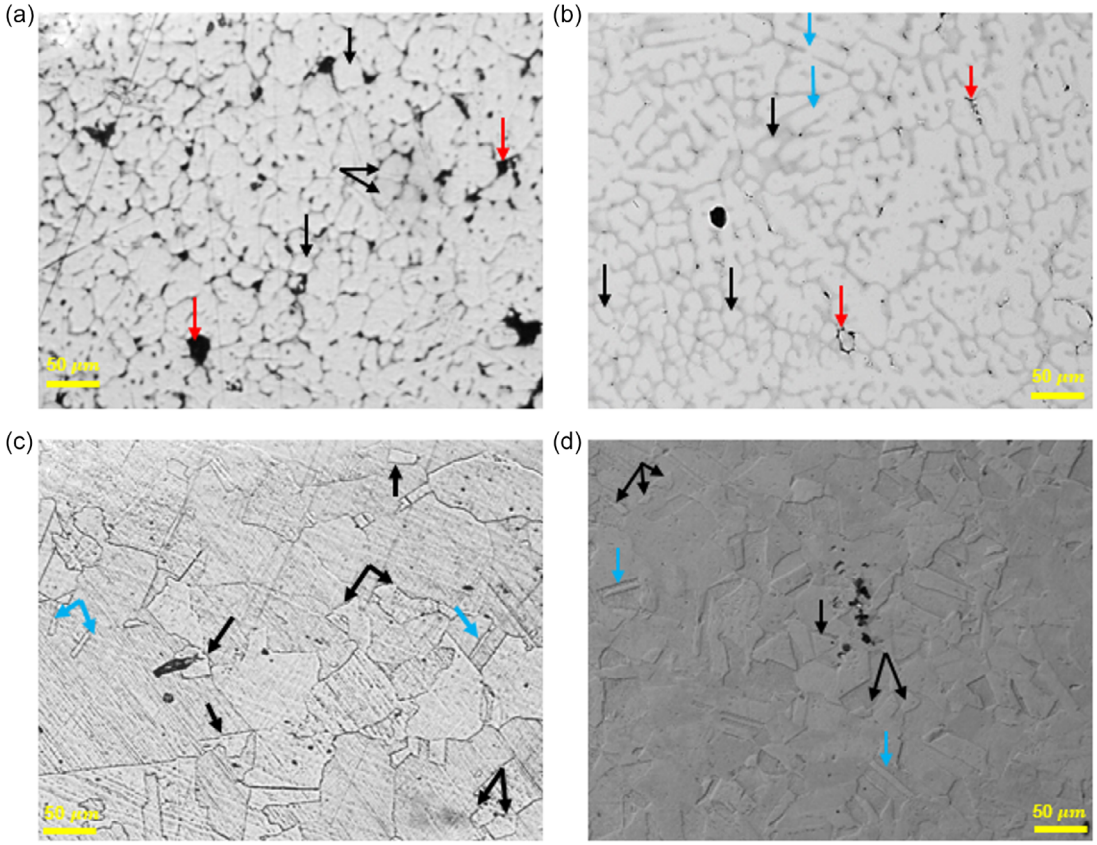

Figure 3. Microstructures of TiNbTaVW and IN718 after deformation at 950 °C/10^{-3} s^{-1}. a) Optical micrograph of TiNbTaVW showing globular grains (black arrows) and voids (red arrows); b) SEM–BSE image of TiNbTaVW showing globular grains (black arrows), elongated grains (blue arrows), and voids (red arrows); c) Optical micrograph of IN718 showing equiaxed grains (black arrows) and elongated grains (blue arrows); d) SEM–BSE image of IN718 indicating elongated (blue arrows) and equiaxed grains (black arrows).

regions of the microstructure. The globular grains also indicate that DRX occurred when the TiNbTaVW RHEA was deformed at 1000 °C. For the IN718 at 1000 °C, equiaxed (blue arrows) and globular (black arrows) grains were observed. A refined grain size of 38.31 ± 7.5 μm was observed compared to 40.3 ± 6.9 μm at 950 °C (Figure 4c,d). No visible cracks or voids are detected in the microstructure of IN718 at 1000 °C.

As the temperature was increased to 1050 °C, the TiNbTaVW RHEA exhibited mostly globular (black arrows) microstructures (Figure 5a,b). A few elongated grains (blue arrows) were observed at 1050 °C, indicating that most elongated grains at 1000 °C had fragmented into smaller globular grains. The presence of more globular grains indicates that the process of dynamic globularization was almost complete as the deformation temperature was increased to 1050 °C. This further signifies that the softening mechanism at 1050 °C is DRX. The grain size (31.43 ± 3.9 μm) of the TiNbTaVW RHEA at 1050 °C is more refined compared to the grain sizes observed at 950 and 1000 °C. Voids were still observed at 1050 °C (Figure 5a,b). Few elongated (blue arrows) and several equiaxed (black arrows) grains were found in many regions of IN718 (Figure 5c,d). This signifies that the DRV and DRX softening mechanisms occur in IN718 at 1050 °C. The grain size of IN718 at 1050 °C is 34.84 ± 3.9 μm, which is more refined than the grains observed at 950 °C and 1000 °C. Micro and huge voids (red arrows) appear in many regions of IN718 at 1050 °C. Some of the voids were found within elongated recrystallized and equiaxed grains.

2.4. Macrostructure of Deformed Samples

Stereo images of the hot deformed TiNbTaVW and IN718 at 950 °C to 1050 °C/10^{-3} s^{-1} are presented in **Figure 6**. Cracks appeared on the TiNbTaVW RHEA's surface at 950–1050 °C (Figure 6a–c). During the hot compression process, stress concentration occurs, leading to an increase in local energy. Once the stress concentration attains a certain threshold, energy is released in the form of cracks. According to Abubaker et al.[22] resultant stress concentration intensifies the creation and spread of microcracks unfavorable to deformation stability. At 950–1050 °C, surface spallation can be observed in the hot deformed IN718 alloy (Figure 6d–f).

2.5. High-Temperature Compression Strength

The high-temperature compression strength of the TiNbTaVW RHEA and the IN718 alloy, compared to other RHEAs and alloys used for high-temperature applications, is depicted in **Figure 7**.

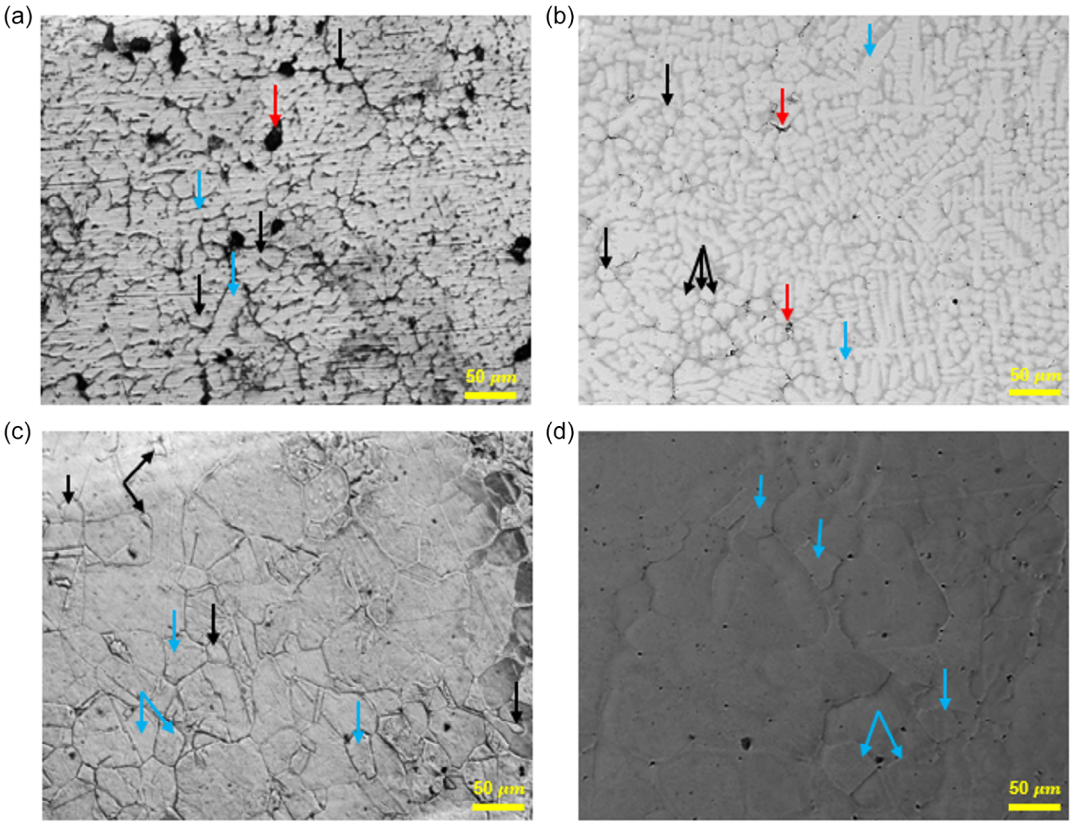

Figure 4. Microstructures of the TiNbTaVW and IN718 after deformation at 1000 °C/10^{-3} s^{-1}. a) Optical micrograph of TiNbTaVW showing globular grains (black arrows), elongated grains (blue arrows), and voids (red arrows); b) SEM–BSE image of TiNbTaVW showing globular grains (black arrows), elongated grains (blue arrows), and voids (red arrows); c) Optical micrograph of IN718 showing equiaxed grains (blue arrows) and globular grains (black arrows); d) SEM–BSE image of IN718 indicating equiaxed grains (blue arrows).

The TiNbTaVW RHEA exhibits higher temperature strengths of 910, 870, and 658 MPa compared to the IN718 alloy, which has 72, 87, and 61 MPa at 950, 1000, and 1050 °C/10^{-3} s^{-1}, respectively. The high-temperature strength of TiNbTaVW RHEA at 950–1050 °C surpasses that of the compared RHEAs and superalloys (Figure 7). However, at 1000 and 1050 °C, the high-temperature strength of TiNbTaVW decreases significantly. According to Yurchenko et al.[51] the loss of strength in RHEAs can be induced by the activation of diffusion-controlled processes.

According to Senkov et al.[52] the decreasing strength of RHEAs at higher temperatures can be attributed to diffusion-controlled processes that start to dominate as the solid solution diminishes. Compared with conventional alloys, RHEAs exhibit a higher softening temperature (0.6–0.8 T_m).[27,53] The high-temperature strength of the TiNbTaVW can be attributed to the addition of high-melting-point elements such as Nb, Ta, and W. The addition of Ta, Nb, and Mo can greatly balance the mechanical properties of RHEAs at higher temperatures.[30,54] Solid solution strengthening effectively functions in RHEAs at temperatures below 1186 °C.[52] Furthermore, the higher-temperature strength of the TiNbTaVW RHEA can also be linked to the considerably larger atomic radii of Ti (1.46Å), Ta (1.46Å), and Nb (1.43Å) compared to the atomic radii of V (1.32Å) and W (1.39 Å). This difference in atomic radii causes lattice distortion, which enhances strengthening via solid solution.[31] High-entropy alloys have excellent high-temperature strength due to the solid solution strengthening effect induced by severe lattice distortion and the thermodynamically favorable high-entropy effect.[30]

The strengthening mechanisms of alloys mainly comprise grain boundary strengthening (Hall-Petch), solid solution strengthening, and second-phase particle strengthening.[7,11,55,56] In this study, the TiNbTaVW RHEA has a single-phase BCC structure, so second-phase particle strengthening (precipitation strengthening and interstitial strengthening) does not exist in the solid solution. Therefore, grain boundary strengthening and solid solution strengthening are expected to be the main strengthening mechanisms. The solid solution strength can be determined as[7,30]

$$\sigma_{cs} = \sigma_{mix} + \sigma_{ss} \quad (1)$$

where σ_{cs} is the compressive strength of the TiNbTaVW RHEA at 950–1050 °C (910, 870, and 658 MPa), σ_{mix} is the individual elemental compressive strength at 950–1050 °C estimated using the rules of mixture, and $\Delta\sigma_{ss}$ is the solid solution strength. The individual elemental high-temperature values at 950–1050 °C for Ti (55, 44, and 37 MPa),[57] Nb (107, 97, and 87 MPa),[58] and Ta (150, 124, and 92 MPa)[59] are considered. Furthermore, the

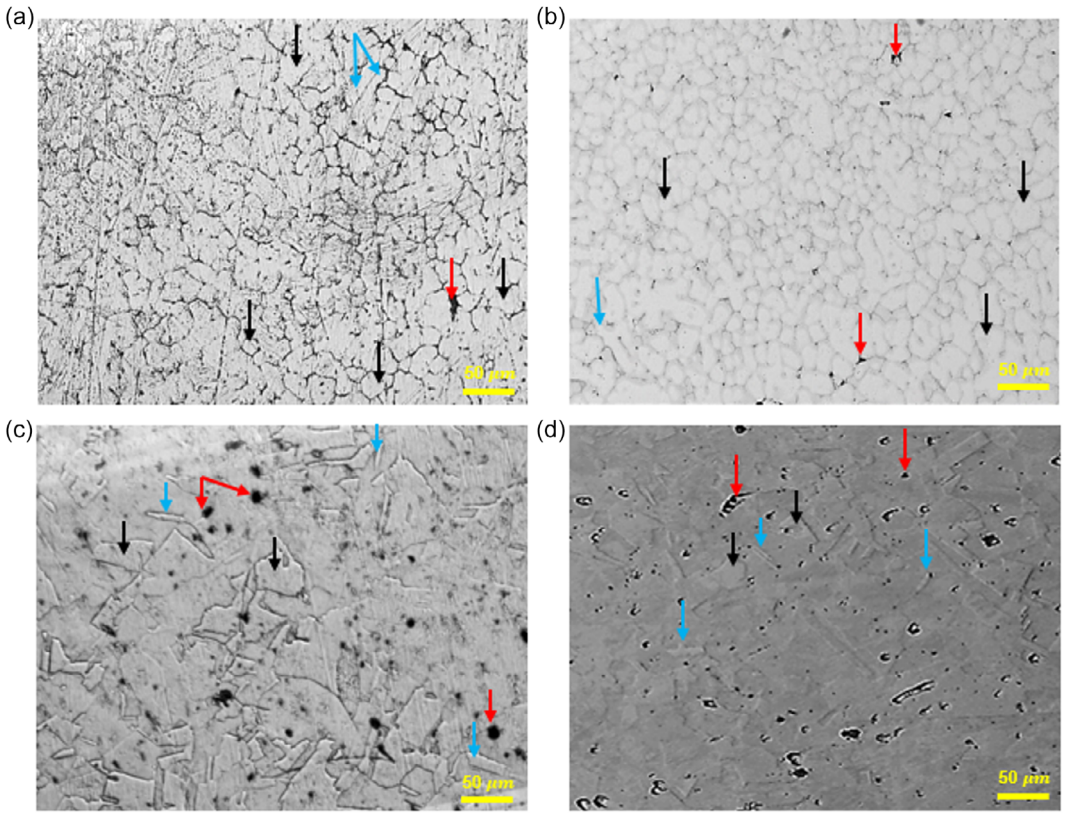

Figure 5. Microstructures of TiNbTaVW and IN718 after deformation at 1050 °C/10^{-3} s^{-1}. a) Optical micrograph of TiNbTaVW showing globular grains (black arrows), elongated grains (blue arrows), and voids (red arrows); b) SEM–BSE image of TiNbTaVW showing globular grains (black arrows), elongated grains (blue arrows), and voids (red arrows); c) Optical micrograph of IN718 showing equiaxed (black arrows), elongated recrystallized grains (blue arrows) and voids (red arrows); d) SEM–BSE image of IN718 indicating equiaxed (black arrows), elongated recrystallized grains (blue arrows) and voids (red arrows).

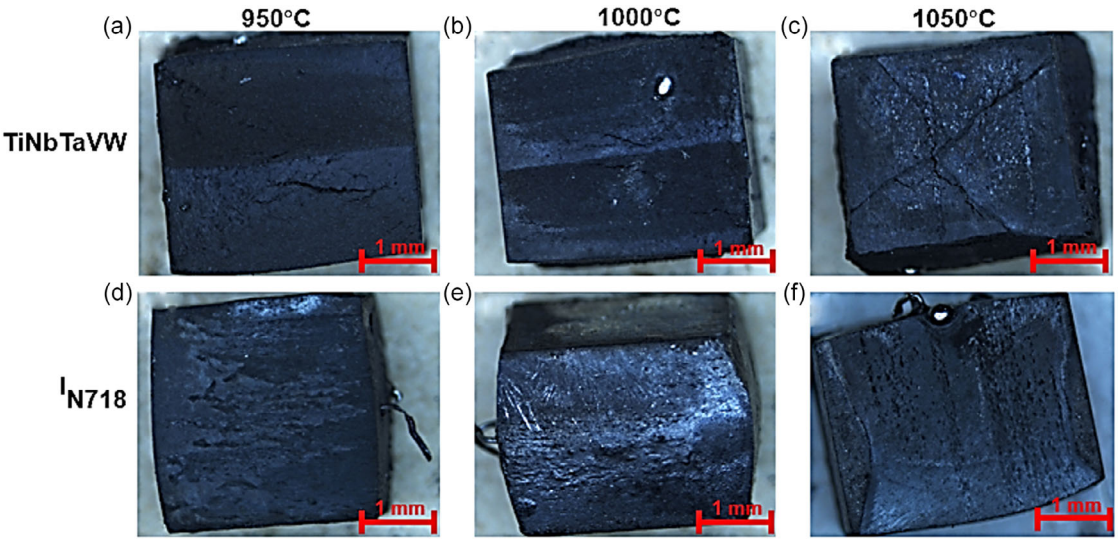

Figure 6. Stereo images of the TiNbTaVW and IN718 surface after deformation at 950–1050 °C/10^{-3} s^{-1}.

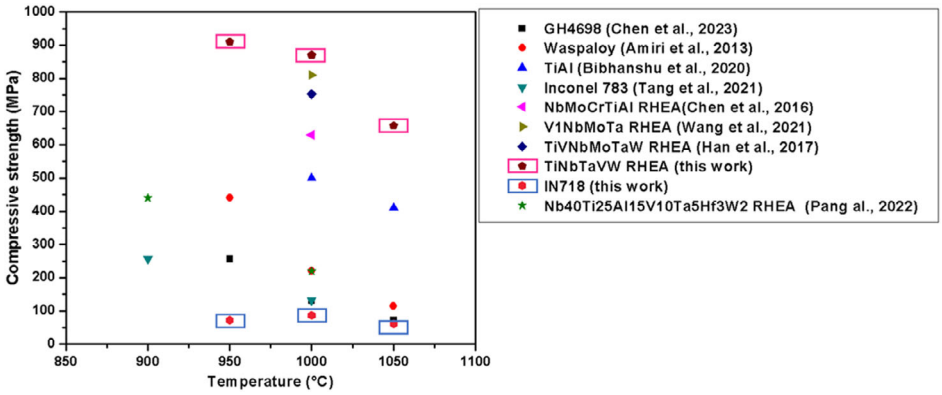

Figure 7. High-temperature strength of TiNbTaVW and IN718 compared to superalloys[77–80] and other RHEAs[23,26,81,82] at 950–1050 °C.

elemental high-temperature values are 155, 79, and 52 Mpa for V[58] and 407, 381, and 324 MPa for W.[60] Using Equation (1), the $\Delta\sigma_{ss}$ is 735, 726, and 538 MPa at 950, 1000, and 1050 °C, respectively.

In addition to solid solution strengthening, the effect of grain size was also considered. Grain boundary strengthening is recognized for its efficiency in grain refining, increasing the strength of polycrystalline metals and alloys.[61] The grain boundary contribution to the strength of the TiNbTaVW RHEA satisfies the temperature dependence of the Hall–Petch relationship as defined in Equation (2).[62]

$$\sigma_{cs}(T) = 120 + 659d^{-0.5} + 597\exp(-T/120) - 0.39Td^{-0.5} \quad (2)$$

where d is the grain size of 44.45, 35.01, and 31.43 μm at temperatures of 950 °C (1223 K), 1000 °C (1273 K), and 1050 °C (1323 K). By substituting the d and T values into Equation (2), the grain boundary contribution to the compressive strength of TiNbTaVW RHEA is 147, 147, and 145 MPa, respectively. It is evident that both solid solution strengthening and grain boundary strengthening contribute to the high-temperature strength of the TiNbTaVW RHEA.

3. Discussion

3.1. Serrations and Sudden Stress Drop Phenomenon

Several softening mechanisms, such as DRV, DRX, dynamic globularization, superplasticity, and flow localization, can occur during hot deformation. Among these mechanisms, DRV, DRX, dynamic globularization, and superplasticity are considered safe, while flow localization, wedge cracking, and adiabatic shear banding are unsafe.[39,63] During the initial stages of deformation, flow stress increases as dislocations interact and multiply. As dislocation density rises, the driving force for recovery also increases.[64] Subsequently, due to the effect of DRX, dislocation density significantly decreases, leading to a gradual drop in flow stress. At 950 °C, the TiNbTaVW RHEA flow curve exhibits a steady-state flow stress followed by a drop in flow stress, indicating the occurrence of DRV and DRX (Figure 2a). At 1000 °C, a broad peak stress followed by a drop in flow stress indicates DRX. At 1050 °C, continuous flow softening was observed, indicating dynamic globularization as the main softening mechanism.[38,39] For the IN718 alloy, steady-state stress was more evident at 950 and 1050 °C, indicating the occurrence of DRV or DRX, while a drop in flow stress at 1000 °C indicates DRX (Figure 2b).

A series of initial peak rises and sudden stress drops were observed in TiNbTaVW and IN718 at 950–1050 °C, which differ from the stress drop phenomenon typically attributed to DRX.[37] Eleti et al.[12] conducted an interrupted hot deformation experiment to elucidate further the reason behind the initial peak rise and sudden stress drop. They found a distinctive drop in the flow stress of the HfNbTaTiZr RHEA around yielding at a strain of ≈0.1, followed by continuous flow softening at 1000–1200 °C/10^{-2}–10^{-4} s^{-1}. An interrupted test conducted at 1000 °C, held for 600 s, and then deformed at a strain rate of 0.001 s^{-1} revealed no clearly observed DRX grains corresponding to the large stress drop. The authors attributed this unusual stress drop to either dislocation unlocking by solute atoms or the ending of short-range ordered structures.

Li et al.[21] also found a stress drop at a strain of ≈0.05 when $Ti_2ZrHfV_{0.5}Ta_{0.2}$ was deformed at 900–1100 °C/10^{-1}–10^{-2} s^{-1}. An interrupted deformation test was carried out at 900 °C/10^{-1} s^{-1}, held for 0 and 600 s intervals, and then deformed at a strain rate of 0.1 s^{-1}. The drop in the flow stress of $Ti_2ZrHfV_{0.5}Ta_{0.2}$ was attributed to dislocation unlocking pinned by a Cottrell atmosphere or short-range order. However, in the TiNbTaVW, the pinning of dislocations by solute atoms or interstitial solute atoms (N and C) is unlikely to occur because it is an equiatomic alloy. The rapid increase in flow stress and subsequent stress drops in TiNbTaVW and IN718 in this study are not caused by dislocation pinning but rather by a change in strain rate at a strain of 0.03–0.035, as depicted in **Figure 8**. The high strain rates (0.06 s^{-1}) at the beginning of deformation, compared to 0.001 s^{-1}, contributed to a rapid increase in flow stress and stress drops observed on the flow curves of the TiNbTaVW RHEA. For IN718, the high strain rates (0.1 s^{-1}) at the beginning of deformation compared to 0.001 s^{-1} led to the rapid increase in flow stress and stress drops observed on the flow curves. Although the overall strain rate remained unaffected, the misleading initial peak rise and stress drops in the flow stress were not a consequence of the microstructural response to the imposed parameters but were due to variations in the hydraulic motion regulating the compression jaws of the Gleeble simulator.

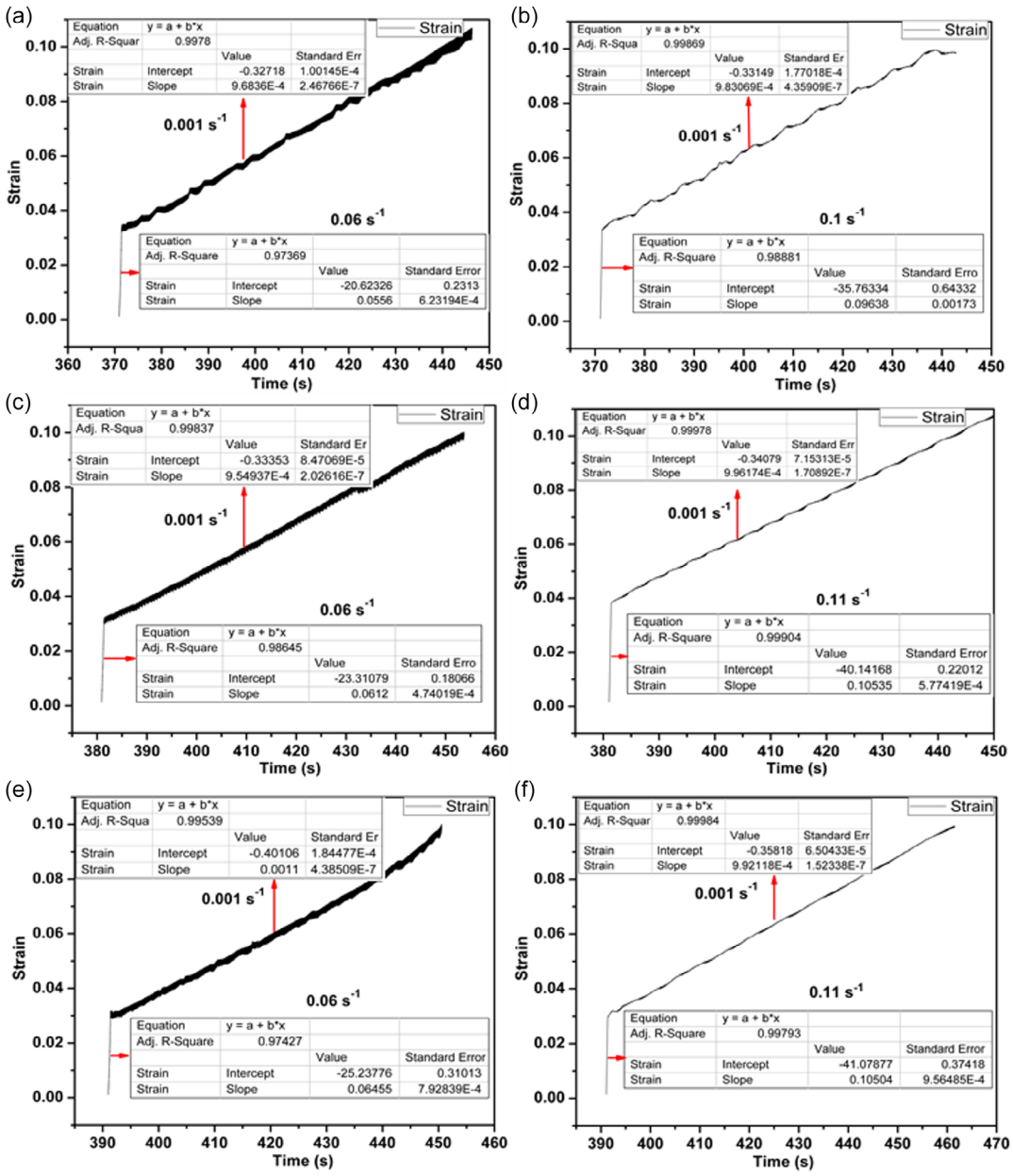

Figure 8. Strain versus time profile at 950 °C/10^{-3} s^{-1} for a) TiNbTaVW and b) IN718. Strain versus time profile at 1000 °C/10^{-3} s^{-1} for c) TiNbTaVW and d) IN718. Strain versus time profile at 1050 °C/10^{-3} s^{-1} for e) TiNbTaVW and f) IN718.

Serrations, characterized by jerky stress–strain curves in solid materials, arise from dislocation motion.[50] It has been observed in flow curves of hot deformed RHEAs such as $Ti_2ZrHfV_{0.5}Ta_{0.2}$,[21] $Al_xNb_{40}Ti_{40}V_{20}$-x,[51] and NbZrTiTa.[20] In the TiNbTaVW RHEA, serrations were seen in both the elastic and plastic regions. At the elastic deformation stage, serrations were observed in the initial peak flow curve of the TiNbTaVW RHEA at 950–1050 °C before the sudden stress drop. Serrated flow stress curves are classified into Type A, Type B, and Type C.[50] The observed serrations in the flow curve of the TiNbTaVW RHEA at the elastic region are similar to Type B.[45,50] Type-B serrations often emerge at the beginning of serrated flow stress, yielding higher temperatures and lower strain rates.[50] Type-B serrations emerge at multiple points along the flow curves, propagate briefly, and then disappear. The elastic region serrations in some RHEAs, like MoNbVTiHf,[65] MoNbTaW,[66] and HfNbTaTiZr,[67] also disappear before the stress drop and are often attributed to machine noise as dislocations at this stage are immobile. Since the serrations occurred at the elastic region in the TiNbTaVW RHEA and dislocation will be immobile at this stage, it can be said that the serrations are a result of machine noise. However, serrations observed in the plastic region of the flow curves of TiNbTaVW at 1050 °C and IN718 at 1000 °C can be attributed to dislocation motion.

Dislocation motion is essential to describe plasticity in crystalline materials as their mobility controls the material's ability to accommodate strain and modify its microstructure.[68]

3.2. Occurrence of Dynamic Recovery and Recrystallization

Grain growth is primarily driven by atomic diffusion and lower strain rates coupled with higher temperatures.[14,20,45] This provides sufficient time and energy for atomic diffusion, facilitating grain boundary movement and eventual grain growth. Globular and elongated grains were observed in the TiNbTaVW alloy at 950 °C, signifying both DRV and dynamic globularization as the softening mechanisms. This corroborates with the flow curve at 950 °C having steady-state flow stress followed by a drop in flow stress. Similarly, at 1000 °C, globular and elongated grains were observed in the TiNbTaVW alloy. However, the flow curve only shows the characteristics of DRX and as confirmed by the globular grains. The occurrence of elongated grains also signifies DRV. Therefore, the softening mechanisms of TiNbTaVW at 1000 °C are still considered DRV and dynamic globularization. The occurrence of both globular and elongated grains has also been observed in the $TiAlVNb_2$ RHEA.[19] At 1050 °C, dynamic globularization is the softening mechanism, as corroborated by the continuous flow softening in the flow curve. Dynamic globularization has been previously reported as a form of DRX.[38,69–72] This mechanism occurs at low strain rates and high deformation temperatures.[44] Equiaxed and elongated grains were observed in IN718 at 950 °C and 1050 °C, as corroborated by steady-state stress, suggesting either DRV or DRX.[42,43] Due to the occurrence of equiaxed and elongated grains, the softening mechanisms for IN718 at 950 and 1050 °C are both DRX and DRV. However, at 1000 °C, mostly equiaxed grains were observed, as corroborated by oscillations and a reduction in the flow curve, signifying DRX. Therefore, DRX is the softening mechanism for IN718 at 1000 °C. The refinement of grains in TiNbTaVW and IN718 is attributed to the characteristics of repeated nucleation and limited growth during DRX. This DRX occurrence promotes grain refinement and reduces deformation resistance in alloys, enhancing their workability and mechanical properties.[14]

Voids were detected near recrystallized grains during the deformation of TiNbTaVW at 950–1050 °C (Figure 3–5). The presence of voids, cracks, and cavities at grain boundaries results from stress concentration, which is more prone to occur at grain boundaries and triple-junction points.[10,73] Under stress loading conditions, cracks propagate along high-angle grain boundaries, resulting in brittle fracture of the alloy in the intergranular region.[74] The higher presence of voids at 950 and 1000 °C compared to 1050 °C may be due to limited dislocation mobility and diffusion,[22,73] which fail to relieve stress concentrations. According to Zhao et al.[75] cracks, voids, and pores can be eliminated with increasing deformation temperature and decreasing strain rate. As the temperature was increased to 1050 °C in TiNbTaVW, the number of voids decreased. However, minipores and large voids were observed in IN718 at 1050 °C (Figure 5c,d), possibly due to stress concentration and inadequate diffusion rates at grain boundaries.[73] Refined grains can impede crack and pore propagation during deformation by increasing the energy barrier required to create new surfaces.[22,76] The TiNbTaVW RHEA at 1050 °C (Figure 5a,b) comprises refined globular grains, which could reduce void propagation.

4. Conclusion

This study investigated the deformation behavior, microstructural evolution, and high-temperature strength of the TiNbTaVW RHEA at 950, 1000, and 1050 °C, with a strain rate of $10^{-3}\,s^{-1}$. This was compared with a commercial-grade nickel-based superalloy, IN718. The following conclusions are drawn from the study. 1) The TiNbTaVW RHEA exhibited a single-BCC phase with a dendritic structure. 2) The TiNbTaVW and IN718 flow curves decreased with an increasing deformation temperature at a constant strain rate. 3) The presence of both globular and elongated grains in the TiNbTaVW alloy at 950 and 1000 °C confirmed that dynamic globularization and DRV are the softening mechanisms. At 1050 °C, mainly globular grains were observed, indicating dynamic globularization as the softening mechanism. In IN718, equiaxed and elongated grains at 950 and 1050 °C suggested both DRX and DRV as the softening mechanisms. At 1000 °C, the dominance of equiaxed grains signified DRX as the only softening mechanism. 4) Voids were found in the microstructure of the TiNbTaVW RHEA at 950 to 1050 °C, whereas minipores and voids were only detected at 1050 °C for the IN718. 5) The TiNbTaVW RHEA has higher-temperature strengths of 910, 870, and 658 MPa, compared to the IN718 alloy, with 72, 87, and 61 MPa at 950, 1000, and 1050 °C/$10^{-3}\,s^{-1}$, respectively. The higher-temperature strength of the TiNbTaVW RHEA can be attributed to both solid solution strengthening and grain boundary strengthening.

This work resulted in an advance by providing a comprehensive analysis of the flow behavior and microstructure of the TiNbTaVW RHEA during hot deformation. By demonstrating comparable or superior performance in specific aspects, the RHEA could be considered in the near future for potential applications traditionally dominated by nickel-based superalloys. This opens new possibilities for RHEAs in high-temperature applications, traditionally dominated by nickel-based superalloys, thereby expanding the material options available for advanced engineering applications.

5. Experimental Section

The TiNbTaVW RHEA was produced through vacuum arc melting under ultrahigh-purity argon gas on a water-cooled copper hearth to obtain an arc-melted alloy. The RHEA was produced using commercial high-purity raw elemental powders comprising Ti (99.7 wt% purity), Nb (99.9 wt% purity), V (99.9 wt% purity), Ta (99.95 wt% purity), and W (99.9 wt% purity) supplied by Weartech (Pty) Limited, South Africa. The TiNbTaVW samples were flipped and remelted three times to ensure chemical homogeneity. Additionally, a nickel-based IN718 superalloy was acquired. Rectangular samples of $6 \times 6 \times 9\,mm^3$ for the hot compression tests were machined using a Gold San CNC wire cutting electrical discharge machining (EDM) machine. The alloys were subjected to hot deformation testing using a Gleeble 3500 thermomechanical simulator. A type R (platinum-rhodium) thermocouple was welded to the midspan of the rectangular test samples using a spot welder to ensure precise temperature control and measurement. Graphite foil and nickel paste were

placed between the Iso-T tungsten carbide anvils and the specimens to reduce friction effects during deformation. Prior to the compression test, the deformation chamber was evacuated to 2.0×10^0 Pa and subsequently filled with inert Ar gas to prevent oxidation.

For each test, the samples were heated to a set deformation temperature of 950, 1000, and 1050 °C at a heating rate of 5 °C s^{-1} and held at this temperature for 180 s to ensure homogenization before compression. The deformation temperatures were chosen based on the hot working conditions of conventional superalloys.[77–79] The samples were deformed at a strain rate of 10^{-3} s^{-1} and a total strain of 0.1, followed by air cooling to retain the microstructure. The TiNbTaVW RHEA was only compressed to a strain of 0.10 due to its brittle nature at high temperatures. The RHEAs that were hot worked at a low strain rate of 10^{-3} s^{-1} included WTaMoNbTi,[29] NbMoCrTiAl,[23] $W_{0.4}MoNb_xTaTi$,[10] AlCrNbTiVZr,[28] and $MoNbVTa_x$.[30] Afterward, the stress–strain data obtained from the hot compression tests were plotted to analyze the shape of the stress–strain curves. For microstructural analysis, the deformed samples were sectioned into two halves, mounted, polished, and then etched in Kroll's reagent. The samples were examined under an Olympus SC50 optical microscope in bright-field mode and a high-resolution Zeiss Sigma field-emission SEM–BSE imaging mode at 15 kV.

Conflict of Interest

The authors declare no conflict of interest.

Author Contributions

Olufemi Sylvester Bamisaye: Conceptualization: (supporting); Data curation: (lead); Formal analysis: (lead); Investigation: (lead); Methodology: (equal); Validation: (equal); Visualization: (lead); Writing—original draft: (lead). **Nthabiseng Maledi**: Conceptualization: (lead); Funding acquisition: (lead); Methodology: (equal); Project administration: (lead); Resources: (lead); Supervision: (lead); Validation: (equal); Writing—review and editing: (lead). **Josias Van der Merwe**: Conceptualization: (lead); Funding acquisition: (lead); Methodology: (equal); Project administration: (lead); Resources: (lead); Supervision: (lead); Validation: (equal); Writing—review and editing: (lead). **Michael Bodunrin**: Conceptualization: (lead); Funding acquisition: (lead); Methodology: (equal); Project administration: (lead); Resources: (lead); Supervision: (lead); Validation: (equal); Writing—review and editing: (lead). **Desmond Klenam**: Contributions Validation: (equal); Writing—review and editing (lead).

Data Availability Statement

The data that support the findings of this study are available from the corresponding author upon reasonable request.

Keywords

dynamic globularization, dynamic recrystallization, elongated grain, hot working, softening mechanism

Received: February 29, 2024
Revised: July 6, 2024
Published online: August 7, 2024

[1] R. C. Reed, in *The Superalloys Fundamentals and Applications*, Cambridge University Press, New York **2006**.
[2] R. Jiang, Y. D. Song, P. A. Reed, *Int. J. Fatique* **2020**, *141*, 105887.
[3] J. W. Yeh, S. K. Chen, S. J. Lin, J. Y. Gan, T. S. Chin, T. T. Shun, C. H. Tsau, S. Y. Chang, *Adv. Eng. Mater.* **2004**, *6*, 299.
[4] O. N. Senkov, G. B. Wilks, D. B. Miracle, C. P. Chuang, P. K. Liaw, *Intermetallics* **2010**, *18*, 1758.
[5] Q. Liu, G. Wang, Y. Liu, X. Sui, Y. Chen, S. Luo, *Mater. Sci. Eng. A* **2021**, *809*, 140922.
[6] D. B. Miracle, O. N. Senkov, *Acta Mater.* **2017**, *122*, 448.
[7] X. W. Nie, M. D. Cai, S. Cai, *Int. J. Refract. Metals Hard Mater.* **2021**, *98*, 105568.
[8] M. Sadeghilaridjani, M. Pole, S. Jha, S. Muskeri, N. Ghodki, S. Mukherjee, *Wear* **2021**, *478–479*, 203916.
[9] O. A. Waseem, H. J. Ryu, O. Ahmed, H. Jin, *J. Alloys Compd.* **2020**, *845*, 155700.
[10] W. Wei, T. Wang, C. Wang, M. Wu, Y. Nie, J. Peng, *Mater. Lett.* **2021**, *295*, 129753.
[11] L. Raman, A. Anupam, G. Karthick, C. C. Berndt, A. S. M. Ang, S. V. S. Narayana Murty, D. Fabijanic, B. S. Murty, R. S. Kottada, *Mater. Sci. Eng., A* **2021**, *819*, 141503.
[12] R. R. Eleti, T. Bhattacharjee, A. Shibata, N. Tsuji, *Acta Mater.* **2019**, *171*, 132.
[13] O. S. Bamisaye, N. Maledi, J. Van der Merwe, D. E. P. Klenam, M. O. Bodunrin, A. D. Akinwekomi, *Manuf. Rev.* **2023**, *10*, 12.
[14] N. N. Guo, L. Wang, L. S. Luo, X. Z. Li, R. R. Chen, Y. Q. Su, J. J. Guo, H. Z. Fu, *Mater. Sci. Eng., A* **2016**, *651*, 698.
[15] Y. Zhang, Y. Liu, Y. Li, X. Chen, H. Zhang, *Mater. Lett.* **2016**, *174*, 82.
[16] F. Dong, Y. Yuan, W. Li, Y. Zhang, P. K. Liaw, X. Yuan, H. Huang, *Intermetallics* **2020**, *126*, 106921.
[17] R. R. Eleti, A. H. Chokshi, A. Shibata, N. Tsuji, *Acta Mater.* **2020**, *183*, 64.
[18] M-l. Hu, W-d. Song, D-b. Duan, Y. Wu, *Int. J. Mech. Sci.* **2020**, *182*, 105738.
[19] Z. C. Bai, X. F. Ding, Q. Hu, M. Yang, Z. T. Fan, X. W. Liu, *J. Alloys Compd.* **2021**, *885*, 160962.
[20] B. Wang, X. Shan, H. Zhao, S. Bai, B. Wang, Y. Tian, Y. Tang, *J. Alloys Compd.* **2023**, *936*, 168059.
[21] T. Li, Y. Lu, Z. Li, T. Wang, T. Li, *Intermetallics* **2022**, *146*, 107586.
[22] M. Abubaker, T. Wang, C. Feng, H. Sun, B. Wang, M. Hamza, M. A. Afifi, W. Liao, *Mater. Des.* **2022**, *222*, 111034.
[23] H. Chen, A. Kauffmann, B. Gorr, D. Schliephake, C. Seemüller, J. N. Wagner, H. J. Christ, M. Heilmaier, *J. Alloys Compd.* **2016**, *661*, 206.
[24] C. Duan, X. Li, E. Werner, *Int. J. Refract. Metals Hard Mater.* **2023**, *115*, 106292.
[25] Y. Jia, L. Zhang, P. Li, X. Ma, L. Xu, S. Wu, Y. Jia, *Front Mater.* **2020**, *7*, 00172.
[26] J. Pang, H. H. Zhang, L. Zhang, Z. Zhu, H. Fu, H. Li, A. Wang, Z. Li, H. H. Zhang, *Mater. Sci. Eng., A* **2022**, *831*, 142290.
[27] O. N. Senkov, C. F. Woodward, *Mater. Sci. Eng., A* **2011**, *529*, 311.
[28] N. Y. Yurchenko, E. S. Panina, G. A. Salishchev, N. D. Stepanov, *Phys. Mesomech.* **2021**, *24*, 642.
[29] Y. Wan, Q. Wang, J. Mo, Z. Zhang, X. Wang, X. Liang, B. Shen, *Adv. Eng. Mater.* **2021**, *2100765*, 00765.
[30] W. Zheng, S. Lü, S. Wu, X. Chen, W. Guo, *Mater. Sci. Eng., A* **2022**, *850*, 143554.
[31] O. S. Bamisaye, N. Maledi, J. Van der Merwe, M. O. Bodunrin, *J. Alloys Compd.* **2024**, *983*, 173803.
[32] W. Huang, J. Yang, H. Yang, G. Jing, Z. Wang, X. Zeng, *Sci. Eng., A* **2019**, *750*, 98.
[33] N. El-Bagoury, M. M. Hessien, M. Alsawat, M. H. H. Mahmoud, A. K. Alanazi, N. A. Alshanbari, *Metallogr. Microstruct. Anal.* **2019**, *8*, 642.
[34] S. Luo, W. Huang, H. Yang, J. Yang, Z. Wang, X. Zeng, *Addit. Manuf.* **2019**, *30*, 100875.
[35] V. A. Popovich, E. V. Borisov, A. A. Popovich, V. S. Sufiiarov, D. V. Masaylo, L. Alzina, *Mater. Des.* **2017**, *131*, 12.
[36] M. J. Luton, C. M. Sellars, *Acta Metall.* **1969**, *17*, 1033.

[37] K. Huang, R. E. Logé, *Mater. Des.* **2016**, *111*, 548.
[38] T. Seshacharyulu, S. C. Medeiros, W. G. Frazier, Y. V. R. K. Prasad, *Mater. Sci. Eng.* **2002**, *A325*, 112.
[39] Y. V. R. K. Prasad, T. Seshacharyulu, *Int. Mater. Rev.* **1998**, *43*, 243.
[40] G. Z. Quan, Y. Wang, Y. Y. Liu, J. Zhou, *Mater. Res.* **2013**, *16*, 1092.
[41] T. Sakai, A. Belyakov, R. Kaibyshev, H. Miura, J. J. Jonas, *Prog. Mater. Sci.* **2014**, *60*, 130.
[42] H. J. McQueen, C. A. C. Imbert, *J. Alloys Compd.* **2004**, *378*, 35.
[43] H. J. McQueen, N. D. Ryan, *Mater. Sci. Eng., A* **2002**, *322*, 43.
[44] M. O. Bodunrin, L. H. Chown, J. W. Van Der Merwe, K. K. Alaneme, *Mater. Sci. Eng., A* **2020**, *791*, 139622.
[45] B. Wang, H. Zhao, X. Shan, Y. Tang, B. Wang, Y. Tian, *Mater. Character.* **2023**, *203*, 113061.
[46] Z. Yu, B. Xie, Z. Zhu, B. Xu, M. Sun, *J. Alloys Compd.* **2022**, *912*, 165220.
[47] J. Brechtl, S. Chen, C. Lee, Y. Shi, R. Feng, X. Xie, D. Hamblin, A. M. Coleman, B. Straka, H. Shortt, R. J. Spurling, P. K. Liaw, *Metals* **2020**, *10*, 10081101.
[48] P. Rodriguez, *Bull. Mater. Sci.* **1984**, *6*, 653.
[49] R. Sharghi-Moshtaghin, S. Asgari, *Mater. Sci. Eng., A* **2008**, *486*, 376.
[50] Y. Zhang, J. P. Liu, S. Y. Chen, X. Xie, P. K. Liaw, K. A. Dahmen, J. W. Qiao, Y. L. Wang, *Prog. Mater. Sci.* **2017**, *90*, 358.
[51] N. Yurchenko, E. Panina, A. Tojibaev, V. Novikov, G. Salishchev, S. Zherebtsov, N. Stepanov, *J. Alloys Compd.* **2023**, *937*, 168465.
[52] O. N. Senkov, J. Gild, T. M. Butler, *J. Alloys Compd.* **2021**, *862*, 100627.
[53] T. M. Butler, O. N. Senkov, M. A. Velez, T. I. Daboiku, *Intermetallics* **2021**, *138*, 107323.
[54] M. Wang, Z. Ma, Z. Xu, X. Cheng, *J. Alloys Compd.* **2019**, *803*, 778.
[55] O. S. Bamisaye, N. Maledi, J. Van der Merwe, M. O. Bodunrin, *Int. J. Refract. Metals Hard Mater.* **2024**, *121*, 106661.
[56] D. G. Kalali, S. Antharam, M. Hasan, P. S. Karthik, P. S. Phani, K. Bhanu Sankara Rao, K. V. Rajulapati, *Mater. Sci. Eng., A* **2021**, *812*, 141098.
[57] Y. Su, F. Kong, F. H. You, X. Wang, Y. Chen, *Vacuum* **2020**, *173*, 109135.
[58] A. N. Behera, R. Kapoor, A. Sarkar, *Int. J. Refract. Metals Hard Mater.* **2024**, *122*, 106711.
[59] F. Zarghani, G. R. Ebrahimi, J. Taheri, H. R. Ezatpour, *Mater. Today Commun.* **2023**, *37*, 107235.
[60] D. Lin, J. S. Han, Y. S. Kwon, S. Ha, R. Bollina, S. J. Park, *Int. J. Refract. Metals Hard Mater.* **2015**, *53*, 87.
[61] W. Huang, S. Yin, X. Wang, R. Guo, Y. Wu, J. Qiao, *J. Mater. Res.* **2023**, *38*, 1719.
[62] S. J. Sun, Y. Z. Tian, H. R. Lin, X. G. Dong, Y. H. Wang, Z. J. Wang, Z. F. Zhang, *J. Alloys Compd.* **2019**, *806*, 992.
[63] D. Mosoma, D. Klenam, T. Maunganidze, M. Bodunrin, *Int. J. Adv. Manuf. Tech.* **2023**, *126*, 2025.
[64] F. J. Humphreys, M. Hatherly, in *Recrystallization and Related Annealing Phenomena*, Elsevier, Oxford **2004**.
[65] G. Meng, R. Gao, F. Liu, J. Yu, *Mater. Today Commun.* **2022**, *33*, 104320.
[66] J. Antonaglia, X. Xie, Z. Tang, C. W. Tsai, J. W. Qiao, Y. Zhang, M. O. Laktionova, E. D. Tabachnikova, J. W. Yeh, O. N. Senkov, M. C. Gao, J. T. Uhl, P. K. Liaw, K. A. Dahmen, *JOM.* **2014**, *66*, 2002.
[67] W. C. Hsu, T. E. Shen, Y. C. Liang, J. W. Yeh, C. W. Tsai, *Acta Mater.* **2023**, *253*, 118981.
[68] E. I. Galindo-Nava, A. Perlade, P. E. J. Rivera-Díaz-Del-Castillo, *Model Simul. Mater. Sci. Eng.* **2014**, *22*, 015009.
[69] X. Li, S. Deng, S. Wang, H. Song, S. Zhang, K. Wang, D. Ouyang, *Mater. Character.* **2021**, *171*, 110749.
[70] D. l. Ouyang, X. Cui, S. q. Lu, H. m. Du, *J. Mater. Res. Technol.* **2020**, *9*, 15662.
[71] C. B. Wu, H. Yang, X. G. Fan, Z. C. Sun, *Trans. Nonferrous Met. Soc. China* **2011**, *21*, 1963.
[72] M. O. Bodunrin, L. H. Chown, J. W. Van Der Merwe, K. K. Alaneme, *Int. J. Adv. Manuf. Tech.* **2019**, *104*, 3017.
[73] S. A. Sajjadi, A. Chaichi, H. R. Ezatpour, A. Maghsoudlou, M. A. Kalaie, *J. Mater. Eng. Perform.* **2016**, *25*, 1269.
[74] W. Huang, X. Wang, J. Qiao, X. Shi, P. K. Liaw, Y. Wu, *Mater. Sci. Eng. A* **2024**, *902*, 146634.
[75] Q. Zhao, F. Yang, R. Torrens, L. Bolzoni, *Materials* **2019**, *12*, 12030457.
[76] B. Xiao, W. Jia, H. Tang, J. Wang, L. Zhou, *J. Mater. Sci. Technol.* **2022**, *108*, 54.
[77] A. Amiri, S. Bruschi, M. H. Sadeghi, P. Bariani, *Mater. Sci. Eng., A* **2013**, *562*, 77.
[78] X. M. Chen, M. T. Ning, H. W. Hu, Y. C. Lin, X. J. Zhou, J. Zhang, X. Z. Lu, J. Chen, Y. X. Liu, *Mater. Character.* **2023**, *201*, 112916.
[79] N. Bibhanshu, A. Bhattacharjee, S. Suwas, *J. Alloys Compd.* **2020**, *832*, 154584.
[80] K. Tang, Z. Zhang, J. Tian, Y. Wu, F. Jiang, *J. Alloys Compd.* **2021**, *860*, 158541.
[81] M. Wang, Z. L. Ma, Z. Q. Xu, X. W. Cheng, *Scr. Mater.* **2021**, *191*, 131.
[82] Z. D. Han, N. Chen, S. F. Zhao, L. W. Fan, G. N. Yang, Y. Shao, K. F. Yao, *Intermetallics* **2017**, *84*, 153.